NTNU

Norwegian University of
Science and Technology

Detached Eddy Simulation of the wake flow behind a model wind turbine

Jan Michael Göing

Master of Science in Mechanical Engineering
Submission date: May 2017
Supervisor: Lars Sætran, EPT

Norwegian University of Science and Technology
Department of Energy and Process Engineering

NTNU

Norwegian University
of Science and Technology

Department of Energy
and Process Engineering

EPT-M-2017-105

MASTER THESIS

for

student Jan Göing

spring 2017

Detached Eddy Simulation of the wake flow behind a model wind turbine

Background and objective

In times of renewable energy development the optimization of the fluid dynamics in offshore wind farms has become an important topic. The fluid-dynamic interaction between the upstream and downstream turbine has become a major field of research. Therein, the application of a yaw angle the upstream turbine is considered to have a high potential for increasing the total power output of a wind farm. Yawing affects the trajectory of the wake behind a turbine and thus leaves more kinetic energy in the wake to be converted by downstream turbines. The wake trajectory and consequently the wind farm power production, however, depend on the ambient wind conditions in the atmospheric boundary layer, such as turbulence intensity, shear and veer.
In order to investigate this effect in more detail, the influence of these physical quantities on the wake behind the yawed turbine should be studied in more detail by the means of a Large Eddy Simulation (LES) using the commercial CFD software ANSYS Fluent. The test cases shall be a reproduction of test cases installed

The following tasks are to be considered:

1. The student should carry out a comprehensive literature study about the topic of wind turbine wake flow and LES and volume of fluid (VOF) modelling.

2. A thorough preparation of the test cases in ANSYS Fluent should be carried out. This includes the construction of the test geometry, mesh generation with ANSYS ICEM and creation of the physical boundary conditions by using user-defined-functions.

3. The main test cases should consist of a non-yawed ($\gamma=0°$) and yawed ($\gamma=30°$) test case for different inflow conditions. The wake flow characteristics are to be validated and compared to a dataset of experimental wind tunnel results at the downstream positions x/D=3 and 6

-- ” --

Within 14 days of receiving the written text on the master thesis, the candidate shall submit a research plan for his project to the department.

When the thesis is evaluated, emphasis is put on processing of the results, and that they are presented in tabular and/or graphic form in a clear manner, and that they are analyzed carefully.

The thesis should be formulated as a research report with summary both in English and Norwegian, conclusion, literature references, table of contents etc. During the preparation of the text, the candidate should make an effort to produce a well-structured and easily readable report. In order to ease the evaluation of the thesis, it is important that the cross-references are correct. In the making of the report, strong emphasis should be placed on both a thorough discussion of the results and an orderly presentation.

The candidate is requested to initiate and keep close contact with his/her academic supervisor(s) throughout the working period. The candidate must follow the rules and regulations of NTNU as well as passive directions given by the Department of Energy and Process Engineering.

Risk assessment of the candidate's work shall be carried out according to the department's procedures. The risk assessment must be documented and included as part of the final report. Events related to the candidate's work adversely affecting the health, safety or security, must be documented and included as part of the final report. If the documentation on risk assessment represents a large number of pages, the full version is to be submitted electronically to the supervisor and an excerpt is included in the report.

Pursuant to “Regulations concerning the supplementary provisions to the technology study program/Master of Science” at NTNU §20, the Department reserves the permission to utilize all the results and data for teaching and research purposes as well as in future publications.

The final report is to be submitted digitally in DAIM. An executive summary of the thesis including title, student’s name, supervisor's name, year, department name, and NTNU's logo and name, shall be submitted to the department as a separate pdf file. Based on an agreement with the supervisor, the final report and other material and documents may be given to the supervisor in digital format.

☐ Work to be done in lab (Water power lab, Fluids engineering lab, Thermal engineering lab)
☐ Field work

Department of Energy and Process Engineering, 15. January 2017

Lars Sætran
Academic Supervisor

Research Advisor: Jan Bartl

Declaration of Authorship

I hereby certify that this thesis has been composed by me and is based on my own work, unless stated otherwise. No other person's work has been used without due acknowledgement in this thesis. All references and verbatim extracts have been quoted, and all sources of information, including graphs and data sets, have been specifically acknowledged.

Date: 10.05.2017 Signature: 

Detached Eddy Simulation of the wake flow behind a model wind turbine

Jan Göing

10th May 2017

Norwegian University of Science and Technology (NTNU) Trondheim,
Technische Universität Berlin (TUB)

Abstract

In times of renewable energy the planning of wind parks and the improvement of the total efficiency has become a major field of research. In order to the optimal positioning of a wind cluster a precise analysis of the wake properties behind a turbine is necessary. Due to the increasing computer performance, numerical models have become an important tool for the precise analysis of the turbulent wake flow. In this study the wake characteristics are calculated with a Delayed - Detached - Eddy - Simulation (DDES) using a sliding mesh technique. The simulation is based on a model wind turbine with a diameter of 0.89 m and a test area which corresponds to the wind tunnel geometry of the department of energy and process engineering from the NTNU. A validation of DDES with an experimental Laser - Doppler - Anemometry (LDA) matches well with the results. The simulation calculates the velocity components and the turbulent kinetic energy sufficiently accurate. In addition, the coherent structure of a vortex shedding and a significant frequency at 1p in the near wake is located with a Proper - Orthogonal - Decomposition. The final part of this report shows the trajectory of the same turbine with a yaw angle of $\gamma = 30°$. This simulation is based on the same numerical conditions as the non yawed operation and describes an unexpected trajectory of the velocity deficit.

1. Introduction

In a wind farm cluster the downstream turbines receive less wind velocity, due to the upstream turbine's extraction of the kinetic energy from the wind. The area of the stream tube behind the turbine increases and a velocity deficit emerges. As a consequence, the downstream turbines cannot produce the same energy as the turbines in the first row of a wind farm.
Researches on wind clusters aim faster free stream velocities for the downstream turbines to enhance the total power output of the wind park. To achieve this aim a detailed understanding about the wake be-

hind the turbine has become a major field of interest and thus to calculate the velocity deficit and other properties of the wake.
Several studies, e.g. those of Larsen [1988] and Katic et al. [1986] developed analytical models to estimate the velocity deficit for the far wake of the turbines. The analytical models are used for the positioning in a wind farm. However, the models have restricted boundary conditions, which influence the correctness of the estimation. Barthelmie and Jensen [2010] investigated the efficiency of a wind farm and the velocity deficit, which depends on the ambient wind conditions, with an increasing efficiency of the wind farm for a higher turbulence intensity.
Rados et al. [2001] constituted an impact on the downstream turbine until twelve diameters, therefore it disables the opportunity to enlarge the distance between the turbines in a large wind farm. As a possibility to enhance the efficiency Ceccotti et al. [2016] and Bartl and Sætran [2016] examined the influence of different tip speed ratios and a changing pitch angle on the downstream turbines. Mühle et al. [2017] and Yuan et al. [2013] described the positive effect on a counter - rotating downstream turbine.
Furthermore, the wake deflection by intentional yaw misalignment remains a major field of research. Adaramola and Krogstad [2011] found out that the wind farm produced significantly more energy with a yawed upstream turbine than with a non - yawed turbine. Gebraad et al. [2016] demonstrated a pronounced wake deflection by a yaw angle of $\gamma = \pm\ 30°$.
Similar to the non - yawed operation, several studies (Jiménez et al. [2008], Gebraad et al. [2016] and Bastankhah and Porté-Agel [2016]) specified the trajectory of the deflected wake and established different kinds of analytical models to estimate the flight path. However, an investigation by Vollmer et al. [2016] showed that the trajectory and shape of the wake also depends on the ambient atmosphere.
Based on the increasing computer efficiency and capacity, the Computational - Fluid - Dynamics (CFD) is an increasingly applied method for wake flow analysis. With CFD the full scale wake can be calculated and the potential of the improvement of the wind farm can be determined.
In this scientific report a high - fidelity CFD simulation on a model wind turbine in a wind tunnel is computed to figure out the full scale wake and to validate the results. The wake is calculated using the Large - Eddy - Simulation (LES) to produce accurate results. However, a study of Piomelli et al. [2003] showed that the accurate resolution of an airfoil boundary layer requires a fine mesh for a LES. To minimize and optimize the computer capacity a Detached - Eddy - Simulation (DES) technique by Spalart et al. [1997] is used. In this method, the boundary layer is modelled with a Reynolds - Averaged - Navier - Stokes - Simulation (RANS) and the free stream is simulated with a LES.
To compare the results with a measurement, the boundary conditions, the turbine and the test areas are based on previous work from Bartl and Sætran [2017]. The simulation includes the geometry of a three bladed rotor with a hub, nacelle and tower. The rotating blades are generated by a sliding - mesh technique. To analyse and discuss the results and the accuracy of the simulation, the velocity components and the turbulent kinetic energy (TKE) are compared to experimental data obtained by a Laser - Doppler - Anemometry (LDA) [Bartl et al., 2017]. To get a detailed analysis and to figure out the limits of the simulation the modes inside of the wake are determined

using Proper - Orthogonal - Decomposition (POD) to detect the coherent structures. In addition, the most significant frequencies are analysed in the wake by calculating the power spectral density (PSD) analysis.
Finally, a second simulation is conducted to identify the trajectory of the wake behind a turbine in yawed operation and to compare the simulation method for this case.

2. Methods

This chapter declares, which kind of methods are used for the simulation and for the validation. At the beginning a short overview of the general information is given. Afterwards, the detailed description of the mesh configuration and the simulation are presented. And at the end, a short outline of the validation process is shown.

2.1. General information

Hereafter, different software and geometries are listed for a better understanding.
In this work the geometry and the mesh are generated with Ansys Inc. v17.2. The simulations are calculated with Ansys Fluent v17.2 on the high performance computer VILJE at the NTNU. For the computation 64 processors are used and the computing time is about 250 hours.
To compare the results, the same rotor is used as in previous studies by Bartl and Sætran [2017]. The diameter D of the rotor is 0.89 m and the profile NREL S826 is used for the airfoil. A new nacelle and tower were constructed to reduce the impact on the wake. A detailed description of the geometry can be found in the report by Sætran et al. [2017]. The turbine is designed for a tip speed ratio of $\lambda = 6$.
The computational domain has the same geometry as the wind tunnel of the department of energy and process engineering at the NTNU and is 2.7 x 1.8 x 11.0 m^3. Bartl and Sætran [2017] described the wind tunnel in more detail. The distance between the rotor and the inlet is about 2D = 1.8 m.
For the post processing Matlab R2014a is applied. For the non - yawed simulation time samples are recorded at 2 kHz. In each time step the rotor is turned by 3.81° and the simulation is calculated for a real time of 1.72 s. The evaluation is started after 0.72 s. For the second investigation the yaw angle γ is changed from 0° to 30° and the sampling frequency is increased to 10 kHz. In this case the rotor is turned by 0.76° for each time step.

2.2. Inflow conditions

In this report two different simulations are conducted. The turbine without yawed operation is investigated in the first case and in the second case the turbine with yawed operation is examined. Both simulations have a non - uniform shear flow as an inflow condition. The non - uniform shear flow is produced by an User - Defined function (UDF) with the power law coefficient α to match the experimental inflow profile (cf. appendix E.1).
The turbulence intensity (TI) and the length scales L_{uu} are generated with the spectral synthesizer by Kraichnan [1970]. The algorithm should be generate a TI of 10% in the ambient flow next to the rotor, due to the TI in the experiment by Bartl et al. [2017]. The general boundary conditions at the inlet are listed in table 1.

Table 1: Inflow conditions of the simulations

No.	Yaw angle γ	Velocity u_{ref} in m/s	α	TI in %	L_{uu} in m
1.	0°	10	11	12	0.1
2.	30°	10	11	12	0.1

2.3. Mesh configuration

In this section the mesh for the calculation is described to make the results reproducible.
The mesh is created in Ansys Icem and consists of 55 $\cdot 10^6$ elements and 30 $\cdot 10^6$ nodes. It is divided in four different parts: rotor, turbine, wake and tunnel domain (cf. figure 2.1). The default grid edge length is placed on 2 cm and a refined mesh for the wake and the domains, which include the turbine, is generated. The rotor domain is shown through the cylinder in figure 2.1. The rotor domain rotates with the rotor and is coupled to the turbine domain via the sliding mesh method (see section 2.4). Due to the complex geometry an unstructured mesh is used for the rotor and turbine domain. The elements are polyhedra, since Juretic [2004] showed that they improve the simulation quality compared to tetrahedra meshes. The remaining part is the tunnel - domain.

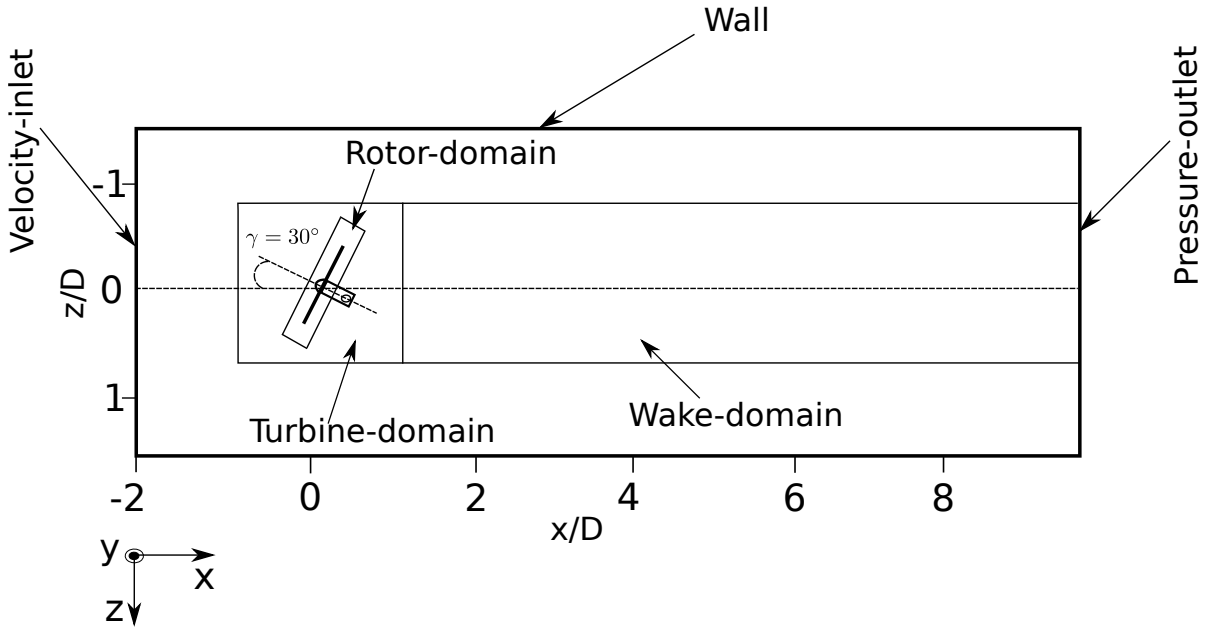

Figure 2.1: Geometry and mesh description of the wind tunnel and the turbine for the second case, the yawed operation

The refined wake area is approximated with the increasing stream tube.
The grid should be able to resolve the Taylor micro scales λ_T, which are the smallest eddies transferring energy (Taylor [1935]). These are calculated with the equation 2.1. Using a sub - grid scale method (cf. section 2.4) the Kolmogorov eddies are modulated, which are the smallest eddies before the dissipation (Kolmogorov [1941]).

$$\lambda_T = \frac{\sqrt{2 \cdot \overline{u'^2}}}{\sqrt{\overline{\left(\frac{\partial u'}{\partial x}\right)^2}}} \tag{2.1}$$

Moreover, the grid should be able to simulate the macro scales Λ. They can be computed with the autocorrelation method.
In figure 2.2 the micro and macro scales of the wake in streamwise direction are demonstrated in different positions from previous experimental data obtained by Hot - Wire Anemometry [Bartl and Sætran, 2017]. The micro scales λ_T are illustrated in the left diagram of figure 2.2. The size of the scales increased after each location. The maximum of each curve is detected in a position z/D = ± 0.5 ± 0.1. The size of the eddies are between 6 and 12 mm. The macro scales Λ are illustrated in the right diagram and have a size between 50 and 120 mm.
In the near wake until x/D = 3 the grid size in radial and tangential direction is refined. In the far wake an isotropic behaviour is expected and the mesh sizes in each direction are equal [Eriksen, 2016].

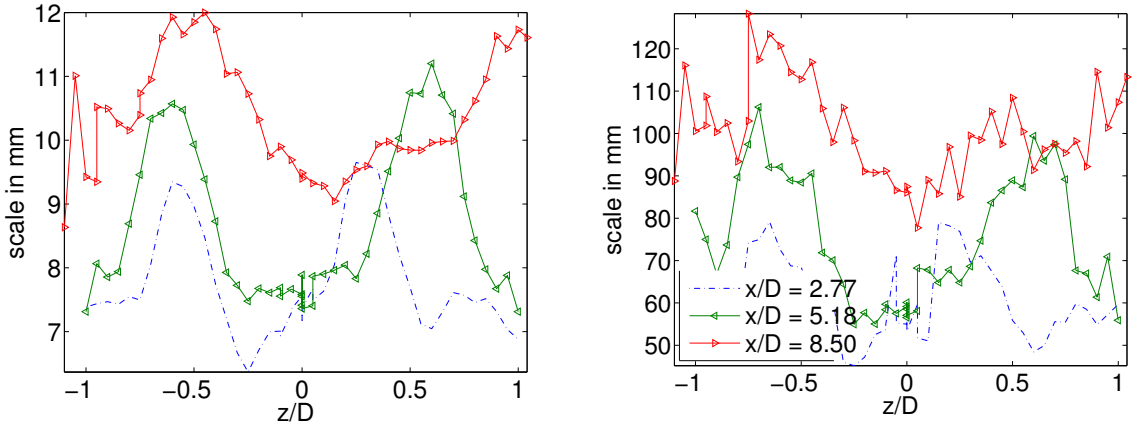

Figure 2.2: Length scales behind a turbine with D = 0.89 m; Left: Micro scales λ_T; Right: Macro scales Λ

The thickness of a boundary layer on the blades is approximated through the boundary layer on a flat plate [Schlichting and Gersten, 2006]. The tip has a thickness of 2 mm, which is in the same range as an investigation by Zhaohui and Selig [2000]. To increase the computer performance and to optimize the number of the cells, the wall function is used for the velocity gradient inside of the boundary layer at the tip position. To implement the wall function in the boundary layer the unitless distance y_+ should be higher than 30, to come out of the buffer region (see appendix D.4). The y_+ - value (cf. equation 2.2) depends on the friction velocity u_*, the viscosity ν and the distance to the first grind in the boundary layer y. To achieve the value the distance

to the first grid in the boundary layer is selected to $5 \cdot 10^{-4}$ m.

$$y_+ = \frac{u_* \cdot y}{\nu} \tag{2.2}$$

2.4. Simulation settings

Hereafter, a short overview of the used simulation techniques and solver algorithm is given.
In this work the 3D incompressible filtered Navier - Stokes - equations without the energy equations are applied to solve the flow outside of the boundary layer regions. The intensive quantity is divided in a low - pass filtered signal $\tilde{\Phi}$ and a high frequency signal Φ'

$$\Phi = \widetilde{\Phi} + \Phi'. \tag{2.3}$$

As a result, after inserting equation 2.3 in the Navier - Stokes - equations, a filtered mass - flux and momentum equation is obtained with the sub - grid scale stress tensor $\tau_{ij} = \widetilde{u_i u_j} - \tilde{u_i}\tilde{u_j}$. The low - pass filtered signal $\widetilde{\Phi}$ is divided with an analytical filter function. Ansys Fluent v17.2 is using the standard rectangle signal for the filtering. For the estimation of stress tensor τ the common Smagorinsky - Lilly method is selected.
Several studies ([Sagmo et al., 2016] and [Bartl and Sætran, 2017]) showed that the modulated quantities in the boundary layer are close to the corresponding experimental data by using the Spalart - Allmaras method for the RANS equations. This method feature is a one - equation turbulence model [Spalart and Allmaras, 1994]. Due to the low mesh quality inside of the boundary layer the Delayed - Detached - Eddy - Simulation (DDES) is chosen, that bounded the LES only outside of the boundary layers [Spalart et al., 2006] and applied the RANS only inside of the boundary layer.
The segregated Pressure - Implicit with Splitting of Operators (PISO) solver is selected to calculate the equations. This method can solve the equation with larger time steps, which is important for the time average of the result.
Based on the flow process, which depends on the down- and upstream behaviour, the bounded central differencing scheme by Leonard [1991] is chosen for the discretization of the momentum. The algorithm is a down- and upwind technique and can be used for structured and non structured meshes.
Finally, the Third - Order MUSCL scheme by van Leer [1979] is selected for the turbulence viscosity ν_τ discretization. This scheme is based on a third order upwind Taylor expansion and is suitable for computing the boundary layer.
The rotor domain rotates with the sliding mesh technique. In this rotating mesh method the grids are not deformed and the quantities are interpolated if there is no connection between the non rotating and rotating grids [Bakker et al., 1997].

2.5. Validation - process

To review the results and to figure out the limits of the simulation different properties of the results are validated and compared to the literature. The different characteristics, which are validated, are defined in this section.
To evaluate the first case, the mean velocity in x - direction (streamwise velocity u), in y - direction (spanwise velocity v) and the TKE are compared to LDA measurements in the locations x/D = 3 and x/D = 6. Based on the two components LDA measuring system [Bartl et al., 2017], the TKE is defined by equation 2.4

$$k = \frac{1}{2} \cdot \left(\overline{u'^2} + 2 \cdot \overline{v'^2} \right). \tag{2.4}$$

The coherent structures and the significant frequencies are filtered out with a POD method by Chatterjee [2000] and PSD for a profound look at the accuracy of the results. The POD technique disassembles a snapshot matrix M of the flow field. The streamwise velocity fluctuation u' in each time step is included on the matrix M. The decomposition is based on the Singular - Value - Decomposition (SVD) according to the equation 2.5

$$M = U \cdot \Sigma \cdot V^T. \tag{2.5}$$

Herein, the physical interpretation of the unitless matrix U, which includes the left eigenvectors, is the spatial mode. The diagonal matrices Σ include the value of the eigenvalues σ, which can be interpreted with the unit of the TKE in m^2/s^2. The matrix V, which includes the right eigenvectors with the unit m/s, is the time mode for the flow field. By phase averaging the angle between the highest time modes V the coherent velocity $\tilde{u}$ can be calculated, which is part of the triple - decomposition (see equation 2.6) by Hussain and Reynolds [1970].

$$u(t,x) = \overline{u}(x) + u'(t,x) + \tilde{u}(t,x) \tag{2.6}$$

To determine the most significant frequency, a PSD is calculated on the first time modes. The pwelch - method with a rectangle window, a sample size of 2000 and a sampling frequency of 2 kHz is used to estimate the PSD.

3. Results

In this chapter the essential results of both simulations are presented and described. At the beginning, the general characteristics of the flow behind a turbine are illustrated and compared to the LDA - measurement with similar boundary conditions. Furthermore, a profound analysis of the velocity in x - direction (streamwise velocity) and y - direction (spanwise velocity), the TKE and the coherent structures are presented. Finally, the trajectory of the wake behind the yawed turbine is compared to the non - yawed operation.

3.1. Flow field comparison

A general overview of the main results are visualized in the figures 3.1 and 3.2. In both figures the normalized mean streamwise u^*, normalized mean spanwise v^* and normalized TKE k^* of the first simulation are compared to the LDA - measurement. The top row of the figures illustrates the results of the non - yawed simulation and the row below shows the results of the corresponding LDA experiment by Bartl et al. [2017].

The results in figure 3.1 are recorded at the downstream position x/D = 3 and the general characteristics of the near wake behaviour are described. The rotor diameter of the turbine is represented as the black circle.

In the first column the normalized mean velocity u^* is shown. The velocity reduction can be described as the velocity deficit behind the turbine. A circular structure with high velocity gradients in the centre and at the edge of the circle are shown as the results of the simulation. Also a nearly axissymmetrical velocity peak is detected inside of the deficit. The slowest velocity u^* is under 0.5 and the fastest u^* is about 0.8. Furthermore, the wake expands until r/D = 0.6.

Compared to the simulation, a velocity deficit with lower velocity gradients at the edge and larger gradients in the centre are demonstrated in the flow field behind the

turbine in the measurement row. Herein, the slowest normalized velocity inside of the deficit is about 0.5 and the fastest is in the range of 0.7. The area of the velocity deficit is nearly the same as in the simulation, with a higher impact on negative y - direction until - 0.6. In both results, the shear flow of the ambiance is pictured outside of the velocity deficit, which has an ordered velocity gradient in the simulation compared to the LDA - results.

In the second column the normalized mean spanwise velocity v^* is illustrated. In the diagram of the simulation three different velocity ranges are detected. Inside of the velocity deficit and in the negative z - direction the average velocity v^* has a positive value (red/yellow) with a maximum about 0.2 and in the positive z - direction the average velocity v^* has a negative value (blue) with a minimum about - 0.2. These areas are connected with a steep velocity gradient and they represent a rotating process. The remaining part outside of the deficit has an average velocity v^* about 0.0 (green).

The second row shows the normalized mean spanwise velocity v^* of the measurement. In contrast to the simulation, the velocity describes a rotation in the full y - z - plane of the wind tunnel. The maximum is about 0.1 and the minimum about - 0.1 of the velocity v^*.

Finally, the normalized TKE k^* is presented in the third column. High levels of TKE indicate a high level of local shear in the flow. The TKE k^* at the edge of the velocity deficit is illustrated in the first row in the third column of the simulation. The k^* level is between 0.01 and 0.03. Furthermore, a lower k^* level is detected in the centre of the velocity deficit. The ambient flow has a level under 0.01. A high k^* in the location of the edge of the velocity deficit with a nearly constant level about 0.025 is described in the results of the measurement. Compared to the simulation, the k^* inside of the deficit has a higher level. The significant difference is the k^* level of the ambience, which is about 0.01 and in the simulation below 0.01.

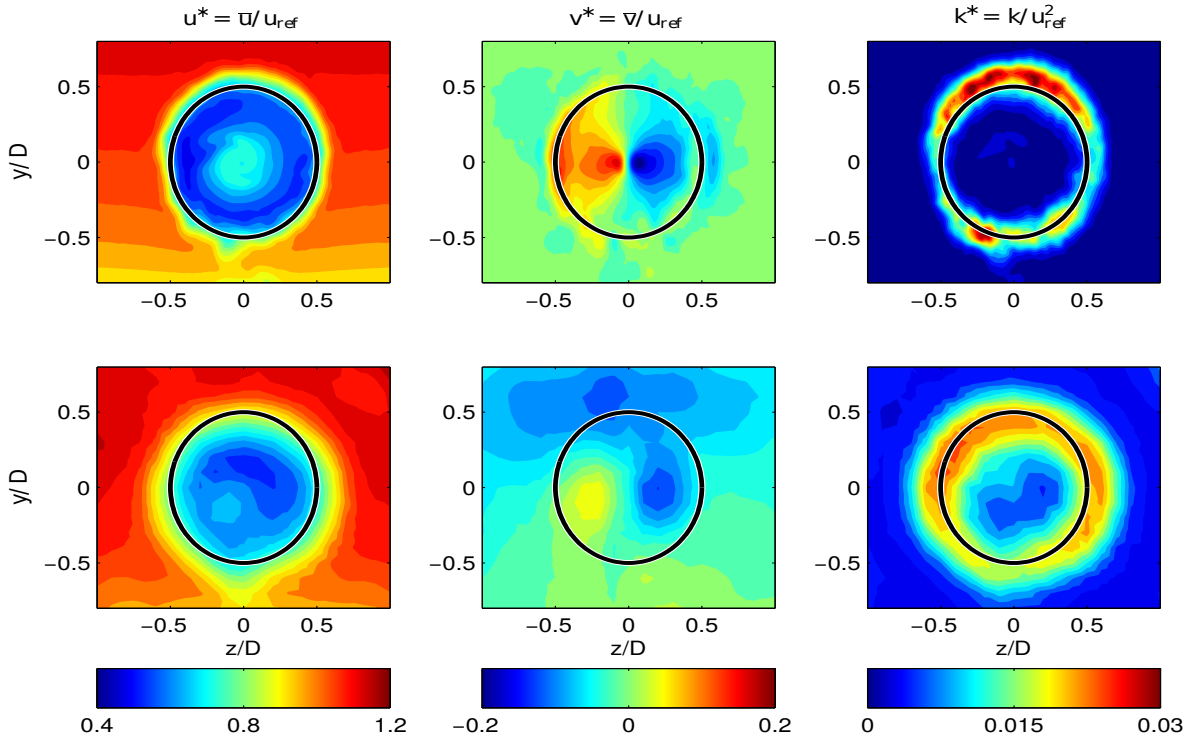

Figure 3.1: Different characteristics of the wake in the y - z - plane at the location x/D = 3 of the first case (non yawed operation). The black circle pictures the rotor diameters. Top: Simulation; Bottom: LDA; Left: normalized mean streamwise velocity u^*; Middle: normalized mean spanwise velocity v^*; Right: normalized TKE k^*

In figure 3.2 the normalized mean streamwise velocity u^*, normalized mean spanwise velocity v^* and the normalized TKE k^* in the y - z - plane at the location x/D = 6 are displayed. In the first row the results of the simulation are illustrated and in the second row the results of the measurement are presented.

A velocity deficit behind a turbine in the area until r/D = 0.68 is shown in the results of the simulation in the first column. The velocity peak inside of the deficit has disappeared and the velocity gradients at the edge are larger compared to the location x/D = 3. The minimum of the velocity level is about 0.6. The velocity u^* of the measurement is illustrated in the second row. The impact of the deficit is detected between y/D = ± 0.6 and z/D = ± 0.7. The slowest velocity is at the same level as the simulation, though with a smaller area. This area is located in the centre. Similar to the first row, the velocity peak disappeared. In contrast to the position x/D = 3, the shape of the deficit has a higher fluctuation and u^* has no clear circular shape in both cases.

The spanwise velocity v^* is demonstrated in the second column. Similar to the previous downstream distance, a rotating flow field is presented in this column. The flow is only rotating inside of the velocity deficit area in the simulation. The maximum of the velocity is detected in the negative z - direction and is close to 0.1. The minimum is close to - 0.1 and is in the positive direction. The average velocity in the ambient flow is similar to the location x/D = 3 and is close to

zero. The velocity v^* of the measurement is shown in the second row. Similar to the first position the ambient air of the cross - section of the wind tunnel is moved around. Apart from that, the maximum and minimum is about $\pm$ 0.05.
The last column displays the TKE k^*, which describes the turbulence of the flow field. Compared to the first position, the k^* peaks merge together until the centre of the simulation. The maximum is about 0.025 and has a similar structure as the measurement. The k^* of the measurement has a maximum about 0.02 and a higher TKE in the ambience flow as the simulation. In both cases the average of the k^* increased and the maximum decreased compared to the position x/D = 3.

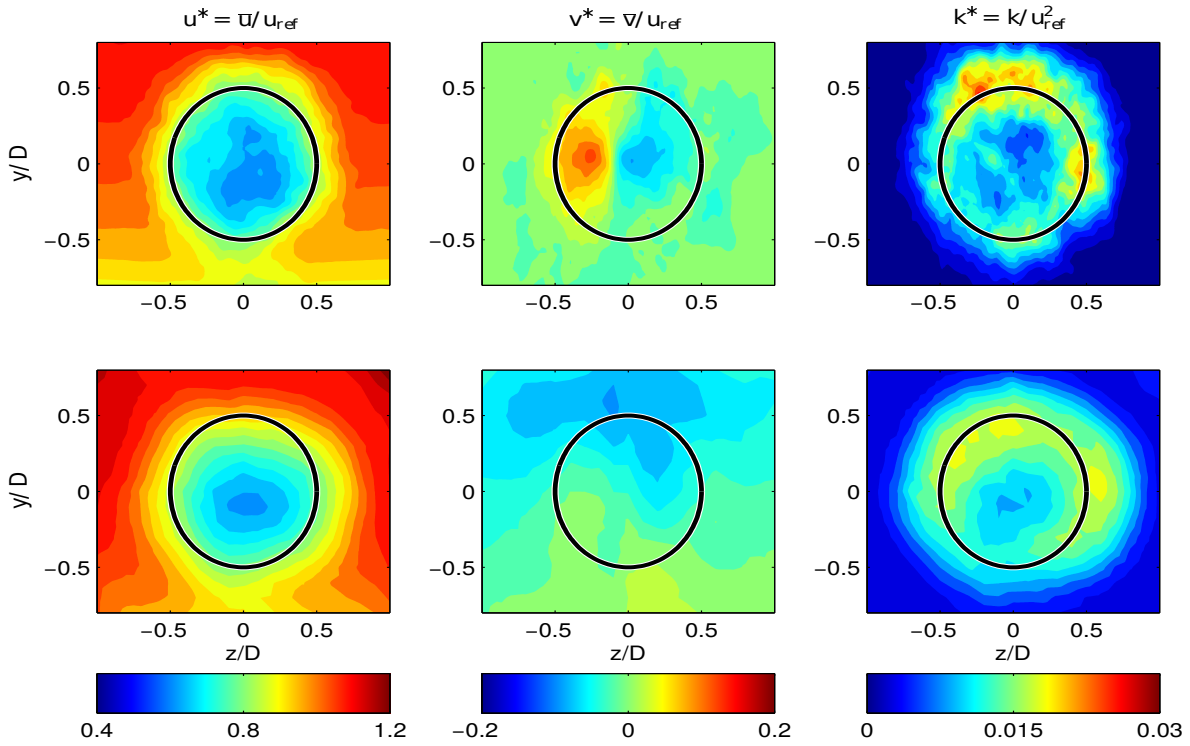

Figure 3.2: Different characteristics of the wake in the y - z - plane at the location x/D = 6 of the first case (non yawed operation). The black circle pictures the rotor diameter. Top: Simulation; Bottom: LDA; Left: normalized mean streamwise velocity u^*; Middle: normalized mean spanwise velocity v^*; Right: normalized TKE k^*

3.2. Normalized mean velocity of the x - and y - components at hub height

To bring out more details of the quantities in section 3.1, the velocity u^* and v^* of the simulation and measurement in the hub height are presented in this chapter. Furthermore, the streamwise velocity u^* is compared to an analytical model.
In figure 3.3 the normalized mean streamwise velocity is displayed in the locations x/D = 3 and x/D = 6. In the diagrams the green line represents the DDES - results, the dashed and dotted blue line illustrates the LDA - results and the dashed black line represents the common analytical gausprofil model by Larsen [1988]. All curves describe the velocity deficit with the free stream velocity in the ambient air in hub height.
In the left diagram, the simulation shows a normalized free stream velocity with a value about 1.08. The slowest velocity inside of the deficit is close to 0.5. Furthermore, a velocity peak until 0.8 is detected near the centre of the deficit. The velocity peak shows an unsymmetrical behaviour. The wake extension is between z/D $\approx\pm$ 0.5.
Afterwards, the free stream velocity of the measurement starts with 1.15 and has a minimum at 0.55. Furthermore, the unsymmetrical velocity peak inside of the deficit has a maximum at 0.65 and the stream tube area is between z/D = $\pm$ 0.6.
Finally, the model by Larsen [1988] has a normalized free stream velocity with the value of 1 and the stream tube area is between z/D = $\pm$ 1. The curve has no velocity peak inside and exhibits a minimum about 0.7 in the centre of the deficit.
The right diagram presents the velocity deficit at the location x/D = 6. The free stream velocity of the green line is about 1.05 and the minimum of the deficit decreased to 0.65. In addition, the velocity gradients are lower and the area of the deficit is between $\pm$ 0.6. The measurement has a similar structure compared to the simulation without a velocity peak inside of the deficit. One difference is detected in the free stream velocity, which is over 1.1 in the measurement and has a higher value than in the simulation.
Finally, the analytical model has a minimum at 0.8 and a low velocity gradient.

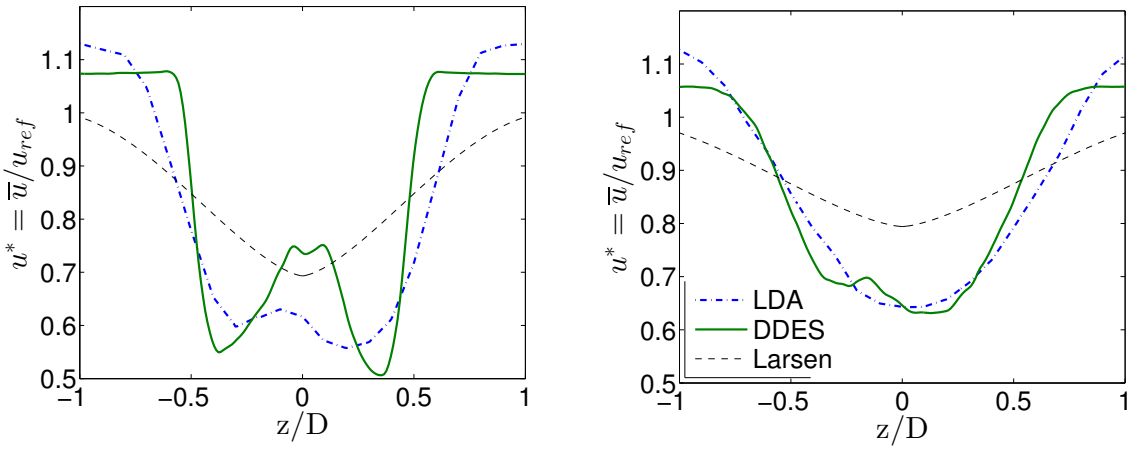

Figure 3.3: Normalized mean streamwise velocity u^* in hub height; Left: in x/D = 3; Right: in x/D = 6

The normalized spanwise mean velocity v^* in x/D = 3 and x/D = 6 of the simulation and the measurement are presented in hub height in figure 3.4. In both diagrams a typical rotating behaviour of the wake is demonstrated.
The green line, which describes the DDES in the left diagram, shows a nearly symmetrical behaviour to the centre. The peaks are located at z/D ≈ ± 0.1. The impact of the velocity is between ± 0.6 and the remaining part has a level of 0.0.
The dashed and dotted blue line describes peak to peak amplitude about 0.1 for the experiment. The peaks are located at z/D = ± 0.25 and have a lower gradient compared to the simulation. The ambience has a constant negative velocity level.
The right diagram displays the spanwise velocity in x/D = 6. The curve of the simulation has a peak in positive and in negative velocity direction. The amplitude of the positive peak is about 0.12 and is located in z/D = - 0.3. The second peak has a velocity about - 0.075 and is positioned in the centre. Furthermore, the level of the ambient velocity is close to zero.
The LDA measurement describes a symmetrical behaviour with a peak to peak amplitude about 0.05 at the position z/D = ± 0.3. Furthermore, the ambient velocity has a negative value.

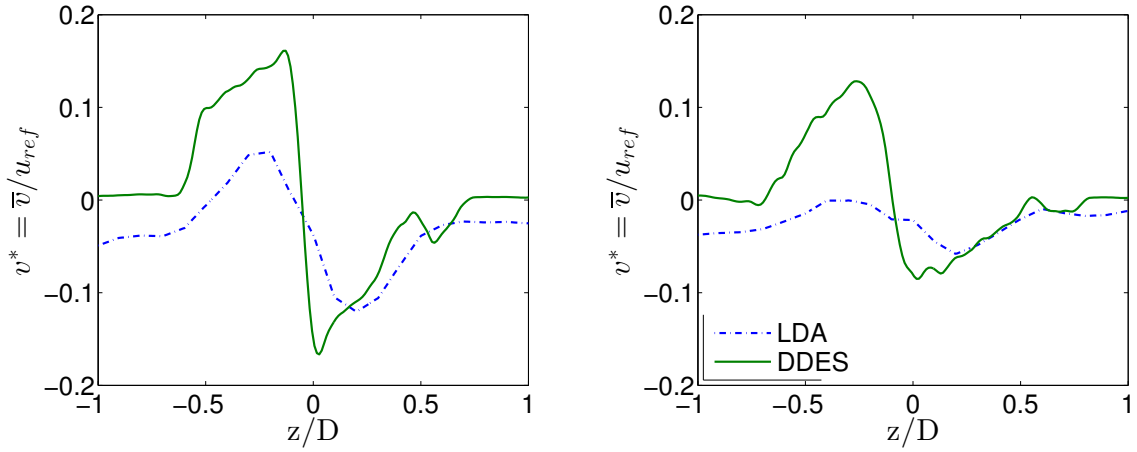

Figure 3.4: Normalized mean spanwise velocity v^* in hub height; Left: in x/D = 3; Right: in x/D = 6

3.3. Turbulent kinetic energy at hub height

To give detailed information of the turbulence behind the turbine the TKE at the locations x/D = 3 and x/D = 6 are presented and compared to the results of the measurement. The normalized TKE in hub height is depicted in figure 3.5. The green line describes the result of the simulation and the dashed and dotted blue line the results of the measurement.
In the left diagram the TKE in the position x/D = 3 is displayed. The DDES is highlighted with two peaks with a level about 0.0175 at the positions z/D = ± 0.5 and the TKE inside of the deficit and in the ambient flow is detected with a level close to zero.
Moreover, the results of the measurement have two peaks with a level about 0.0225 at the same position as the DDES. A noticeable difference to the simulation is the

higher level of the TKE in the centre and ambient air. The TKE inside of the deficit is between 0.008 and 0.012 and the level in the ambient flow is close to 0.005.
The TKE in the location x/D = 6 is illustrated in the right diagram. In contrast to the first location, the level of the TKE is in the same range between the simulation and the measurement. In both cases the peaks are located at z/D = ± 0.6 with a value about 0.016 and 0.018. The level of the TKE is about 0.001 in the centre. Furthermore, two peaks are significantly broader and stretch out until z/D = ± 1.

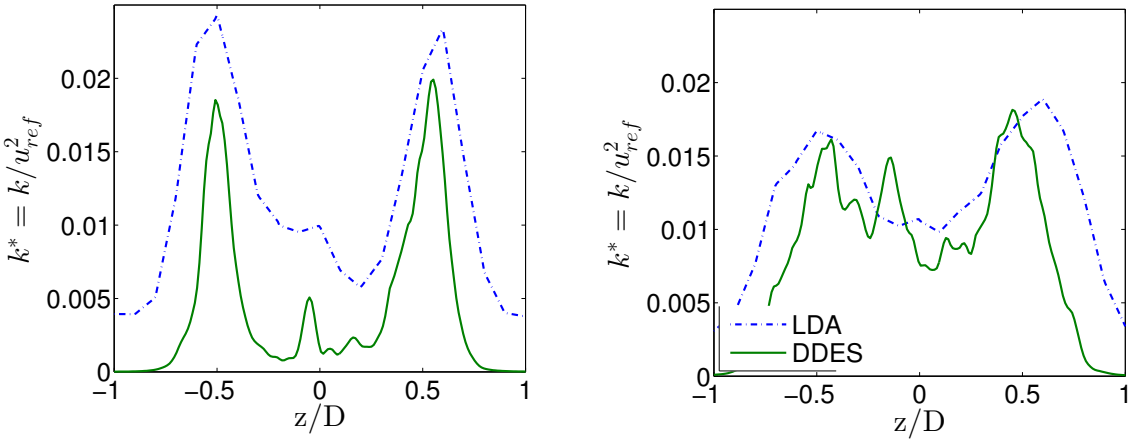

Figure 3.5: Normalized turbulent kinetic energy k^* in hub height; Left: in x/D = 3; Right: in x/D = 6

3.4. Coherent structures and significant frequencies

To investigate the coherent velocity $\tilde{u}(t, x)$ of the triple decomposition (see equation 2.6) and the significant frequency in the streamwise velocity u the POD - technique is applied at the positions x/D = 1, x/D = 3 and x/D = 6.
After a SVD of the snapshot matrix M, the values of the eigenvalues of the flow field are listed in the diagonal matrix Σ. The physical interpretation of the eigenvalues are the TKE, which are illustrated in the left diagram of figure 3.6 at the location x/D = 1. The diagram displays the first 150 important normalized eigenvalues. A steep gradient at the beginning is visible in the curve. The normalized TKE of the first mode is 8 % and of the second mode is 7 %. Furthermore, the diagram explains that the first few modes have the highest impact on the total TKE and on the flow field (the locations x/D = 3 and x/D = 6 are listed in B.2). Each eigenvalue has a right and left eigenvector. The right eigenvector (or time mode V) includes information about the frequency spectrum (see figure 3.8).
In right diagram of figure 3.6 the normalized second time mode V_2^* over the first normalized time mode V_1^* is presented at the location x/D = 1. A phase shifted behaviour between these both modes is described in the diagram by the dotted closed circle.

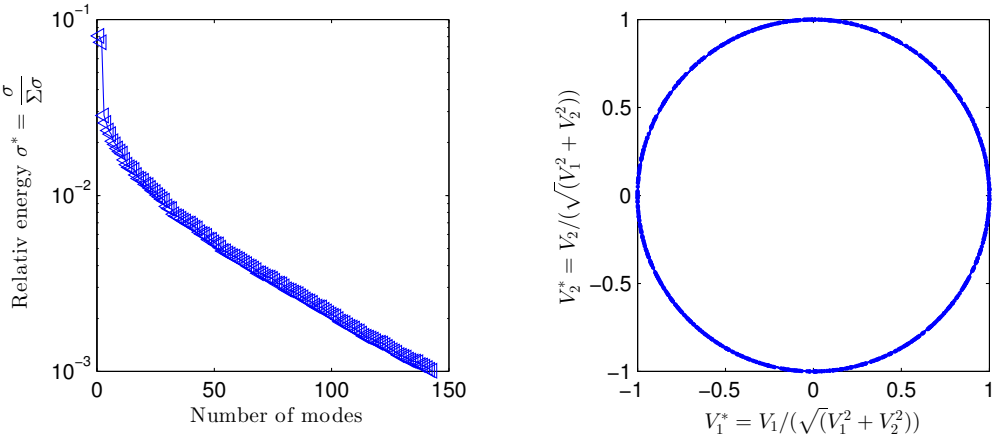

Figure 3.6: POD analysis in x/D = 1; Left: Relative energy of the modes; Right: Interaction between the V_1^* and V_2^*

Moreover, the circle can be used to calculate the phase angle between the first and second mode and the phase average. The difference between the phase average and the mean velocity is the value of the coherent velocity $\tilde{u}(t, x)$. The same process can be done for the other positions.
The normalized coherent velocity $\tilde{u}^*$ of the streamwise velocity u in the position x/D = 1, x/D = 3 and x/D = 6 are demonstrated in figure 3.7. The left diagram shows the velocity in x/D = 1. Two circles next to the edge of the blades are detected. They are located between r/D = 0.53 and r/D = 0.63. The first circle (red/yellow) has a positive and the second (blue) a negative velocity. Furthermore, a significantly weaker $\tilde{u}^*$ is detected in the centre of the wake.
The two circles with the changing signs are also shown in the diagram in the middle (x/D = 3). They are located between r/D = 0.42 and r/D = 0.68. The lines of the circle are wider and have a higher spatial variation. The right diagram shows the coherent velocity in the position x/D = 6. In contrast to the other locations, the clear circles are dispersed. However, the diagram shows also a changing sign in the $\tilde{u}^*$.

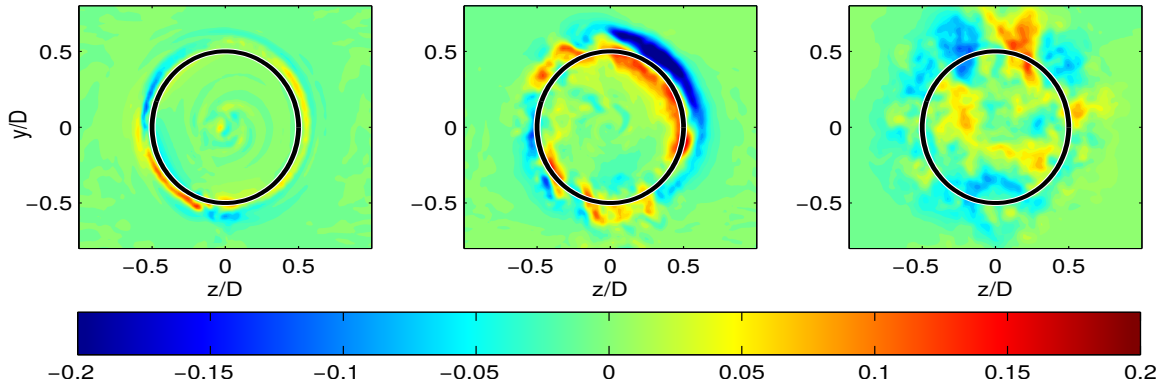

Figure 3.7: Coherent normalized streamwise velocity $\tilde{u}^*$ of the phase average between V_1 and V_2. The black circle pictures the rotor diameter. Left: x/D = 1; Middle: x/D = 3; Right: x/D = 6

Moreover, the time modes V include the fluctuation information of the streamwise velocity $u(t, x)$ and can be used for a frequency analysis. Due to the short time average of the simulation, a low frequency cannot be detected with a point frequency analysis.
The power spectral density estimation PSD over the logarithmic Strouhal number St of the first time mode V_1 in the locations x/D = 1, x/D = 3 and x/D = 6 are shown in figure 3.8. The Strouhal number is the normalized frequency with the rotor diameter D and the reference velocity u_{ref}.
In the left diagram the normalized frequency (blue line) and the Kolmogorov - 5/3 law (black line) in the location x/D = 1 are displayed. The - 5/3 law describes the typical curve of the isotropic area of a turbulence flow. A significant peak at St = 1.9 at the position x/D = 1 is detected. This is the frequency of the 1p. Furthermore, the frequency decreases after the peak with a similar behaviour as the - 5/3 law.
A similar curve can be detected in the diagram in the middle. This diagram illustrates the PSD at the position x/D = 3 of the first mode V_1.
The right diagram shows the PSD in the location x/D = 6 of the first mode with no significant peak.

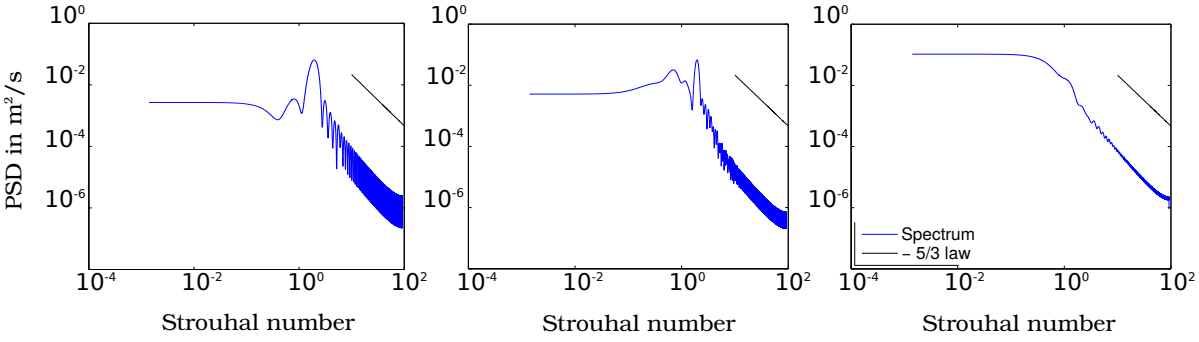

Figure 3.8: Spectra of the mode V_1; Left: x/D = 1; Middle: x/D = 3; Right: x/D = 6

3.5. Yaw cases

This chapter describes an investigation about the simulation of the second case. In this case the trajectory of the velocity deficit behind a turbine in a yawed operation with the angle $\gamma = 30°$ is examined.
A top view of the normalized mean streamwise velocity in the z - x - plane in hub height is demonstrated in figure 3.9. In both diagrams the shape and trajectory of the velocity deficit is detected. In the top diagram the normalized mean streamwise u^* of the non - yawed operation is presented. The dashed black line describes the centreline of the deficit, which shows a constant line and thus no lateral wake. Furthermore, the area of the stream tube starts between z/D = ± 0.55 in x/D = 1 and expands to z/D = ± 0.61 at the position x/D = 6.
The velocity u^* in yawed operation is illustrated in the diagram below. The non axissymmertical velocity deficit at the position x/D = 1 is between z/D = 0.54 and z/D = - 0.83 . The range increases at the location x/D = 6 to z/D = 0.58 to z/D = - 0.75.
The yawed operation shows a different trajectory compared to the normal case. The

flight path describes an asymmetrical behaviour. Furthermore, the wake has a greater impact on the negative direction. The centreline of the deficit is described with the dashed black line. In x/D = 3 the centreline is in the position of z/D = - 0.12 and in x/D = 6 at the position of - 0.18. An analytical centreline, based on a model for yawed operation by Jiménez et al. [2008], is displayed as a blue line. A thrust coefficient c_T equal to 0.6 is selected, due to the results of Adaramola and Krogstad [2011].

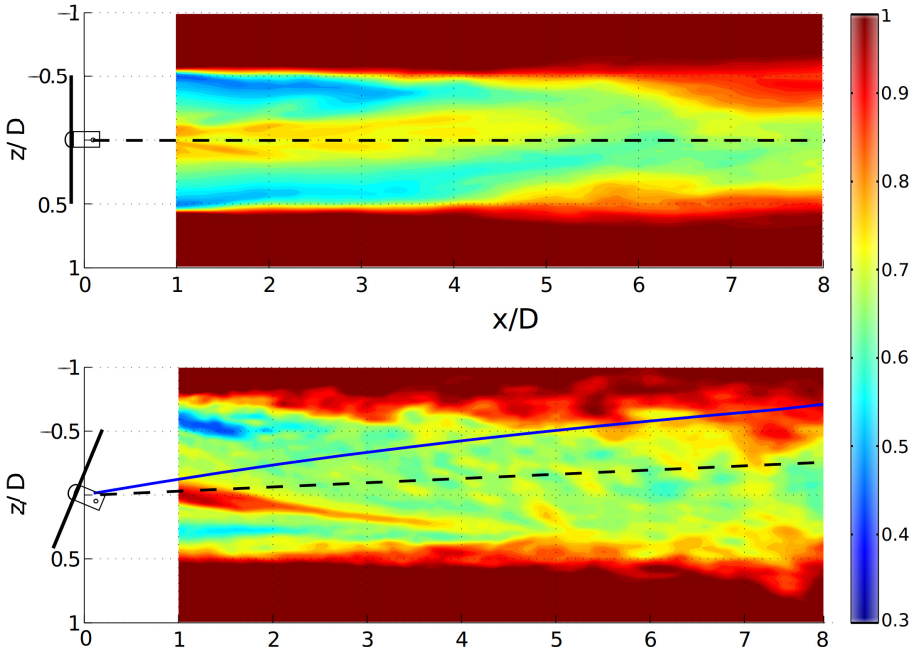

Figure 3.9: Contours in z - x - planes of the normalized streamwise velocity in a top view at hub height. The blue line describes the centreline approximation and the dashed black line illustrates the centreline of the simulations. Top: velocity u^* non - yaw operation; Bottom: velocity u^* yaw operation

4. Discussion

By the means of a CFD analysis the full wake behind a turbine is calculated and the important characteristics of the wake are extracted to discuss the accuracy and the limits of the DDES with the sliding mesh method.
Troldborg et al. [2009] divided the wake in two different parts: the near wake, which includes the potential core and information about the tip vortex, and the far wake behind the potential core.

In the beginning of this chapter the results of the streamwise velocity u^*, the spanwise velocity v^* and the TKE k^* in the y - z - plane and in the hub height of the near wake and far wake are discussed and compared with corresponding experimental measurements and results from literature.
A part of the near wake is displayed in figure 3.1, due to the clear circular structure and the low TKE level inside of the wake, which describes the potential core. In contrast to the measurement, the centre of the wake has a considerable lower TKE level.

Furthermore, the TKE level in the ambient flow has the same value as in the centre of the deficit in both cases. This difference can be attributed to the inlet. Here the simulation starts with a TI about 1% instead of the 12%. A reason for the too weak TI in the inflow is the used spectral synthesiser algorithm, which generated the TI in the inflow. On the other hand, the work group CD - Adapco in the previous work by Bartl and Sætran [2017] has successfully applied this method.
This mismatch can be a reason for the small difference of the velocity deficit (see left diagram of figure 3.3). This assumption is based on an investigation by Bartl and Sætran [2017]. They measured a significant asymmetrical velocity peak until $u^* = 0.8$ and a velocity deficit under 0.6 in the location in x/D $\approx$ 3, behind a turbine with the same rotor, a TI = 0.24% and without a shear flow in the inflow. In addition, they came to the result, that the TI has a higher impact on the velocity deficit as a shear flow in the inflow conditions.
In contrast to the analytical model by Larsen [1988], the velocity deficit of the simulation has a closer correspondence to the measurement in the area of the stream tube and the velocity level.
In the next part of this study, the spanwise velocity v^* is compared to the measurement in figure 3.4. One reason for the overestimation of the spanwise velocity v^* in the near wake is a negative spanwise velocity in the inflow of the experiment. This influence may not be evidenced in the simulation and is a conclusion of the method, which generates the shear flow in the experiment.
The next property of the near wake is the TKE. It corresponds with the measurement in the location of the maxima and is in the same range of the TKE level. A mismatch of the TKE level inside of the wake can be reduced to the low inflow TI. Also Bartl and Sætran [2017] measured a TKE under 0.01 in x/D $\approx$ 3.
Troldborg et al. [2009] defined the far wake with a dispersing influence of the tip vortex and an increasing shear flow in the wake. This process can be detected in the results of the position x/D = 6. The streamwise velocities of the simulation and measurement describe a decreasing deficit, compared to the location x/D = 3. Both deficits have a high correspondence (cf. right diagram of figure 3.3), compared to the analytical model, which overestimates the deficit.
One difference is detected in the free stream velocity, which is higher than one, due to the blockage effect in the wind tunnel. The mesh grid next to the wind tunnel wall has a low mesh quality ($y_+ > 100$), due to the optimising of the computer performance, which could not calculate the increasing thickness of the boundary layer exactly. In the analytical model the blockage effect is not included.
Similar to the first location, the spanwise velocity in the right diagram of figure 3.4 overestimates the maximum and minimum peaks.
Finally, the TKE of the simulation corresponds well with the level and location with the measurement (cf. figure 3.2). However, the TKE of the simulation indicates a higher spatial variation as the TKE of the measurement.

The next part of this section discusses the coherent structures and significant frequencies.
The coherent velocity $\tilde{u}(t, x)$ demonstrates the vortex shedding of tip vortices from the blade tips in the near wake (cf. the left and middle diagram of figure 3.7). The Hot - Wire investigation by Lynum [2013], located different tip vortices only in the

distance x/D = 1. They are in a range between r/D = 0.55 and 0.62. The Hot - Wire investigation by Eriksen and Krogstad [2017] figured out the process of the coherent velocity in streamwise direction. They measured some tip vortices between r/D = 0.55 and 0.59 in x/D = 1 and between a tip vortex r/D = 0.43 and r/D = 0.72 in x/D = 3. The increasing structures, which are also detected in the POD of the DDES, are a consequence of the merged tip vortices in the distance of x/D = 3 [Eriksen and Krogstad, 2017]. Both studies used the same rotor and a low TI = 0.24%. These locations of the tip vortex correspond with results of the DDES.
In addition, an indication of the root vortices is displayed in the left diagram of figure 3.7.
The significant frequency of the first time modes in the near wake (x/D = 1 and x/D = 3) is about 1p. Therefore, it can be concluded that the coherent structure has the main frequency about 1p in the near wake.
Eriksen [2016] found out that the frequency of 1p has an influence on the flow until x/D = 5. The study shows, that the frequency 1p is in the range about r/D = 0 to r/D = 0.725 in the location x/D = 1 and in the location x/D = 3 range about r/D = 0.45 to r/D = 0.9. The coherent structures of the simulation appear in these ranges.
Furthermore, the study describes a significant frequency about 3p at x/D = 1, which cannot be found in the simulation.
The results of the first case (non yawed operation) demonstrate that the DDES is able to calculate the velocity deficit, the rotation and shear flow of the wake which shows a good match with the experimental measurements and literature. Furthermore, the simulation shows some specific characteristics of the wake, which correspond well with previous studies. On the other hand, the full spectra and significant 3p frequency are not detected.

In the last part of this report the trajectory of the velocity behind a turbine is investigated. The centreline of the deficit, in yawed operation, has a significant difference to the analytical model. The second diagram of figure 3.9 shows an increasing impact on the velocity deficit in the negative z - direction, which is the reason for the shifted centreline. The border between the deficit and the free stream velocity in the positive z - direction is nearly constant. In an investigation with similar conditions by Adaramola and Krogstad [2011] and Loland [2011] the trajectory has a clearly deflected behaviour after a location of x/D = 1. Also the studies by Bastankhah and Porté-Agel [2016] and Howland et al. [2016] illustrated a deflected trajectory about z/D = 0.4 in a location of x/D = 5 with an angle of $\gamma = + 30°$. The deflected wake depends on the thrust force, which has possibly a too low dissolution on the rotor. Furthermore, the impact between the wall function and the thrust force is not entirely investigated yet.

5. Conclusion

This study revealed some significant aspects of wake modelling with a DDES and the sliding mesh technique. The report examined the characteristics in the near and far wake area behind a turbine with different yaw angles (0° and + 30°).
The method was able to simulate the streamwise, spanwise velocity and the TKE behind a turbine without yawed operation at different downstream distances. The results of the simulation match well with the experimental results.

Furthermore, the coherent structure and the significant frequency of the flow behind the turbine reflected the expected value compared to the literature. The coherent structure in the near wake exhibits a tip and root vortex and the significant frequency is about 1p.
The last part of this report focused on the trajectory of the wake in yawed operation and computed a slight deflected deficit.
However, the DDES simulation differs from experimental measurements in some points. In the near wake the velocity deficit has a significant impact on the tower and the spanwise velocity overestimated the results of the experiment. Furthermore, the TKE has a lower level in the centre of the deficit and in the ambient air compared to the experiment.
In the far wake, the velocity and the TKE correspond with the experiment. In a few points the results of this work had a higher spatial variation as in the experiment, which might be due to the short simulation time. Furthermore, the 2p and 3p is not detected in the PSD of the time modes of the POD. Compared to previous studies, the trajectory of the velocity deficit behind a turbine in yawed operation described an unexpected behaviour, due to a not significantly deflected flight path. Based on the results, no statement can be made about the increasing efficiency of a wind park.
A number of possible reasons for deviations in the DDES simulations are discussed. The velocity peak and the low TKE inside of the near wake could be a consequence of the too weak TI in the inflow and ambient air.
Furthermore, a negative spanwise velocity in the inflow conditions of the experiment could be the reason for the overestimation of the spanwise velocity of the simulation in the near and far wake.
The short time average of the simulation could be the trigger of the higher spatial variations in the far wake.
Finally, there are some causes for the unexpected trajectory of the wake behind a turbine in yaw operation. Firstly, the dissolution of the boundary layer could be too weak to compute the thrust force accurately. Furthermore, the time step for the simulation could be too high for an exact force dissolution. Both properties depend on the computer capacity, which was limited in this study.
Consequently, a number of improvements are proposed for future studies of this issue. To improve the boundary conditions, a UDF should be generated the TI in the inlet and the simulation should be run for a longer time to produce a longer time average.
Furthermore, the numerical condition of the second case should be optimised. The grid next to the turbine can be refined to get a higher dissolution of the thrust force distribution and the y_+ - value should be reduced under one to model the boundary layer exactly.

References

Adaramola, M. S. and Krogstad, P. Å. [2011], 'Experimental investigation of wake effects on wind turbine performance', *Renewable Energy* **36**, 2078–2086.

Bakker, A., Laroche, R. D., Wang, M. H. and Calabrese, R. V. [1997], 'Sliding mesh simulation of laminar flow in stirred reactors', *Institution of Chemical Engineers* **75**, 3–5.

Barthelmie, R. J. and Jensen, L. E. [2010], 'Evaluation of wind farm effi ciency and wind turbine wakes at the Nysted offshore wind farm', *Wind Energy* **13**, 573–586.

Bartl, J., Mühle, F., Schottler, J., Hölling, M., Peinke, J., Adaramola, M. and L, S. [2017], 'Experimental study on the wake behind a yawed wind turbine model exposed to different turbulent inflow conditions', *manuscript submitted to Wind Energy Science* .

Bartl, J. and Sætran, L. [2016], 'Experimental testing of axial induction based control strategies for wake control and wind farm optimization', *Journal of Physics: Conference Series* **753**, 32–35.

Bartl, J. and Sætran, L. [2017], 'Blind test comparison of the performance and wake flow between two in - line wind turbines exposed to different turbulent inflow conditions', *Wind energy science* **2**, 55–76.

Bastankhah, M. and Porté-Agel, F. [2016], 'A wind-tunnel investigation of wind-turbine wakes in yawed conditions', *Journal of Physics: Conference Series* **625**, 12–14.

Boussinesq, J. [1872], 'La Theorie des raux courantes'.

Ceccotti, C., Spiga, A., Bartl, J. and Sætran, L. [2016], 'Effect of Upstream Turbine Tip Speed Variations on Downstream Turbine Performance', *Energy Procedia* **94**, 478–486.

Chatterjee, A. [2000], 'An introduction to the proper orthogonal decomposition', *Computational Science* **78**, 808–817.

Eriksen, P. [2016], 'Rotor wake turbulence', *Doctoral thesis (NTNU)* .

Eriksen, P. and Krogstad, P. [2017], 'Development of coherent motion in the wake of a model wind turbine', *Renewable Energy* **108**, 449–460.

Gasch, R. and Twele, J. [2005], *Windkraftanlagen Grundlagen, Entwurf, Planung und Betrieb*, Vol. 4, Springer - Verlag, Berlin Heidelberg.

Gebraad, P. M. O., Teeuwisse, F. W., van Wingerden, J. W., Fleming, P. A., Ruben, S. D., Marden, J. R. and Pao, L. Y. [2016], 'Wind plant power optimization through yaw control using a parametric model for wake effects a CFD simulation study', *Wind Energy* **19**, 95–114.

Hansen, M. O. L. [2008], *Aerodynamics of Wind Turbines*, Vol. 2, Earthscan, London UK.

Howland, M. F., Bossuyt, J., Meyers, J. and Meneveau, C. [2016], 'Wake structure in actuator disk models of wind turbines in yaw under uniform inflow conditions ,', *Journal of Renewable and Sustainable Energy* **8**, 1–17.

Hussain, K. M. F. and Reynolds, W. C. [1970], 'The mechanics f an organized wave in turbulent shear flow', *Journal of Fluid Mechanics* **41**, 241–258.

Jiménez, Á., Crespo, A., Migoya, E. and Garcia, J. [2008], 'Large-eddy simulation of spectral coherence in a wind turbine wake', *Environmental Research Letters* **3**.

Juretic, F. [2004], 'Error analysis in finite volume CFD', *Doctoral thesis (Imperial College London)* p. 233.

Katic, I., Højstrup, J. and Jensen, N. O. [1986], 'A simple model for cluster efficiency', *European Wind Energy Association* .

Kolmogorov, A. N. [1941], 'Dissipation of Energy in the Locally isotropic Turbulence', *Annals and Magazine of Natural History* **19**, 393–405.

Kraichnan, R. [1970], 'Diffusion by a Random Velocity Field', *The physics of fluids* **13**, 22–31.

Larsen, G. [1988], 'A simple wake calculation procedure'.

Launder, B. E. and Spalding, D. B. [1974], 'The numerical computation of turbulent flows', *Computer methods in applied mechanics and engineering* **19**, 269–289.

Leonard, B. [1991], 'The ULTIMATE conservative difference scheme applied to unsteady one dimensional advection', *Computer Methods in Applied Mechanics and Engineering* **88**, 17–74.

Loland, K. M. [2011], 'Wind Turbine in Yawed Operation', *Masterthesis (NTNU)* .

Lynum, S. [2013], 'Wind turbine wake meandering', *Masterthesis (NTNU)* .

Mühle, F., Adaramola, M. and Sætran [2017], 'The effect of rotational direction on the wake of a wind turbine rotor a comparison study of aligned co– and counter rotating turbine arrays', *ScienceDirect* pp. 18–20.

Piomelli, U., Balaras, E., Pasinato, H., Squires, K. D. and Spalart, P. R. [2003], 'The inner-outer layer interface in large-eddy simulations with wall-layer models', *International Journal of Heat and Fluid Flow* **24**, 538–550.

Rados, K., Larsen, G., Barthelmie, R., Schlez, W., Lange, B., Schepers, G., Hegberg, T. and Magnisson, M. [2001], 'Comparison of Wake Models with Data for Offshore Windfarms', *Wind Engineering* **25**, 271–280.

Reynolds, O. [1883], 'An Experimental Investigation of the Circumstances Which Determine Whether the Motion of Water Shall Be Direct or Sinuous, and of the Law of Resistance in Parallel Channels', *Royal Society* **174**, 935–982.

Sætran, L., Mühle, F., Bartl, J., Schottler, J. and Adaramola, M. S. [2017], Invitation to the 2017 Blind test 5 workshop The wake behind a yawed wind turbine.

Sagmo, K., Bartl, J. and Sætran, L. [2016], 'Numerical simulations of the NREL S826 airfoil', pp. 1–9.

Schlichting, H. and Gersten, K. [2006], *Grenzschicht - Theorie*, Vol. 10, Springer - Verlag, Berlin Heidelberg.

Schwarzer, R. [2014], *CFD - Modellierung*, Vol. 1, Springer - Verlag, Berlin Heidelberg.

Spalart, P. R. and Allmaras, S. R. [1994], 'A one-equation turbulence model for aerodynamic flows', *La Recherche Aerospatiale* **1**, 5–21.

Spalart, P. R., Deck, S., Shur, M. L., Squires, K. D., Strelets, M. K. and Travin, A. [2006], 'A new version of detached-eddy simulation, resistant to ambiguous grid densities', *Theoretical and Computational Fluid Dynamics* **20**, 181–195.

Spalart, P. R., Jou, W. H., Strelets, M. and Allmaras, S. R. [1997], 'Comments on the feasibility of LES for wings and on a hybrid RANS/LES approach', *Advances in DNS/LES* **1**, 4–8.

Taylor, G. I. [1935], 'Statistical Theory of Turbulence'.

Troldborg, N., Sørensen, J. N. and Mikkelsen, R. F. [2009], 'Actuator line

modeling of wind turbine wakes', *Doctoral thesis (DTU)* .

van Leer, B. [1979], 'Towards the Ultimate Conservative Difference Scheme.', *Journal of Compitational Physics* **32**, 101–136.

Vollmer, L., Steinfeld, G., Heinemann, D. and Kühn, M. [2016], 'Estimating the wake deflection downstream of a wind turbine in different atmospheric stabilities: An LES study', *Wind Energy Science Discussions* pp. 129–141.

Yuan, W., Ozbay, A., Tian, W. and Hu, H. [2013], 'An Experimental Investigation on the Effects of Turbine Rotation Directions on the Wake Interference of Wind Turbines', *American Institute of Aeronautics and Astronautics* pp. 1–16.

Zhaohui, D. and Selig, M. S. [2000], 'The effect of rotation on the boundary layer of a wind turbine blade', *Renewable Energy* **20**, 167–181.

Appendix

A. List of Symbols

Roman letters

Symbol	Unit	Definition
A	m^2	Area of the rotor
D	m	Diameter
E	J	Energy
f	hz	Frequency
G	-	Analytical filter function
k	m^2/s^2	Turbulent kinetic energy
m	kg	Mass
$\dot{m}$	kg/s	Mass flux
n	hz	Rotation speed
p	Pa	Pressure
P	W	Power
R	m	Radius
t	s	Time
T	N	Thrust
u	m/s	Velocity in x - direction, streamwise velocity
U	-	Spatial mode
u_*	m/s	Velocity in the boundary layer
v	m/s	Velocity in y - direction, spanwise velocity
V	m/s	Time mode
w	m/s	Velocity in z - direction
W	m/s	Induction velocity
y	m	Distance to the first grid in the boundary layer
x, y, z	m	Cartesian coordinates

Greek letters

Symbol	Unit	Definition
γ	$^\circ$	Yawed angle
κ	-	Karman constant
λ	-	Tip speed ratio
λ_T	m	Taylor micro scale
Λ	m	Taylor macro scale
μ	Pas	Dynamic viscosity
ν	m^2/s	Kinematic viscosity
ν_τ	m^2/s	Turbulent viscosity
Φ	-	Intensive quantity
ρ	kg/m^3	Density
σ	-	Eigenvalue
Σ	-	Diagonal - matrix of eigenvalue
τ	m^2/s^2	Stress tensor
τ_w	m^2/s^2	Wall shear stress

Special numbers

Symbol	Defintion	Name
C_μ	-	Coefficient in approximated turbulent transport equations
c_P	$\frac{P}{0.5 \cdot A \cdot u_1^3 \cdot \rho}$	Power coefficient
c_T	$\frac{T}{0.5 \cdot A \cdot u_1^2 \cdot \rho}$	Thrust coefficient
St	$\frac{D \cdot f}{u_{ref}}$	Strouhal number
y_+	$\frac{u_* \cdot y}{\nu}$	Unitless wall distance

Indices

Index	Definiton
x^*	Normalized quantities
$\overline{x}$	Mean quantities
x'	Fluctuation or high frequency quantities
$\tilde{x}$	Coherent or low frequency quantities
x_a	Ambient quantities

Acronyms

Acronyms	Definition
CFD	**C**omputational **F**luid **D**ynamic
DES	**D**etached **E**ddy **S**imulation
DDES	**D**elayed **D**etached **E**ddy **S**mulation
LDA	**L**aser **D**oppler **A**nemometry
LES	**L**arge **E**ddy **S**imulation
NREL	**N**ational **R**enewable **E**nergy **L**aboratory
NTNU	**N**orges **T**eknisk **N**aturvitenskapelige **U**niversitet
PISO	**P**ressure **I**mplicit with **S**plitting of **O**perator
POD	**P**roper **O**rthogonal **D**ecomposition
PSD	**P**ower **S**pectral **D**ensity
RANS	**R**enolyds **A**veraged **N**avier **S**tokes
TI	**T**urbulence **I**ntensity
TKE	**T**urbulent **K**inentic **E**nergy
TUB	**T**echnische **U**niversität **B**erlin
UDF	**U**ser **D**efined **F**unction

B. Additional Results

To complete the results, the velocity w^*, the eigenvalues of the first case are listed in this chapter. Furthermore, the normalized streamwise, spanwise velocity and TKE of the second case are demonstrated in the location x/D = 3 and x/D = 6.

B.1. Velocity in z - direction

The mean normalized velocity w^* in z - direction is displayed in figure B.1.

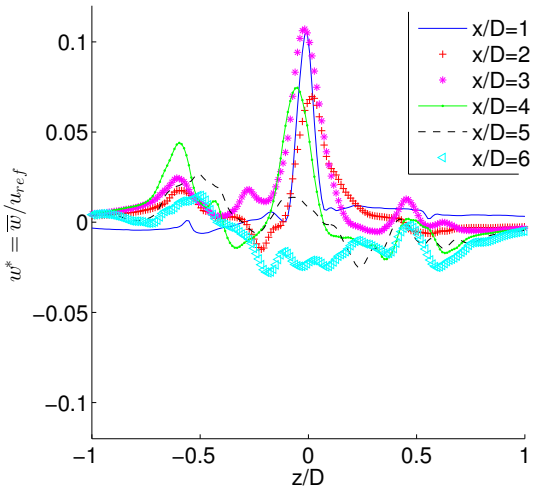

Figure B.1: Normalized mean velocity w^* in x/D = 1 until 6 of the first case in hub height

B.2. POD - eigenvalues of the different locations

The figure B.2 shows the normalized eigenvalue of flow field in x/D = 3 and x/D = 6.

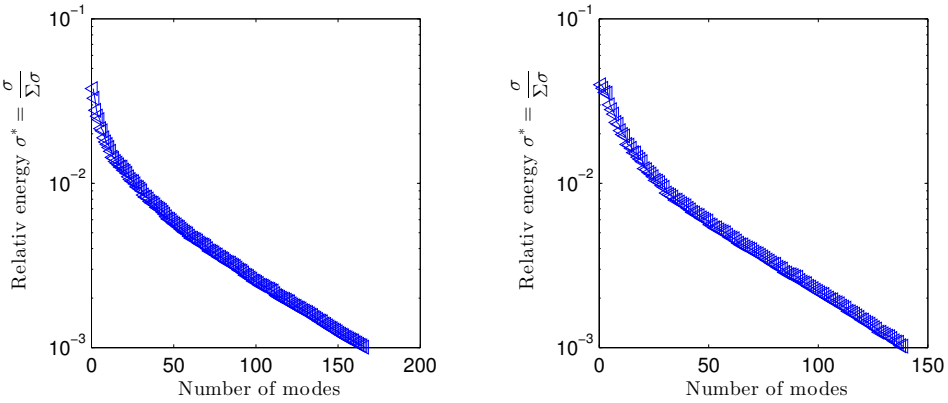

Figure B.2: Normalized eigenvalues σ^* of the snapshot matrix M. Left: x/D = 3; Right: x/D = 6

B.3. General characteristics of the flow field in yawed operation

The following diagrams in figure B.3 describe the normalized mean streamwise, spanwise velocity and TKE in x/D = 3 and x/D = 6 of the yawed simulation.

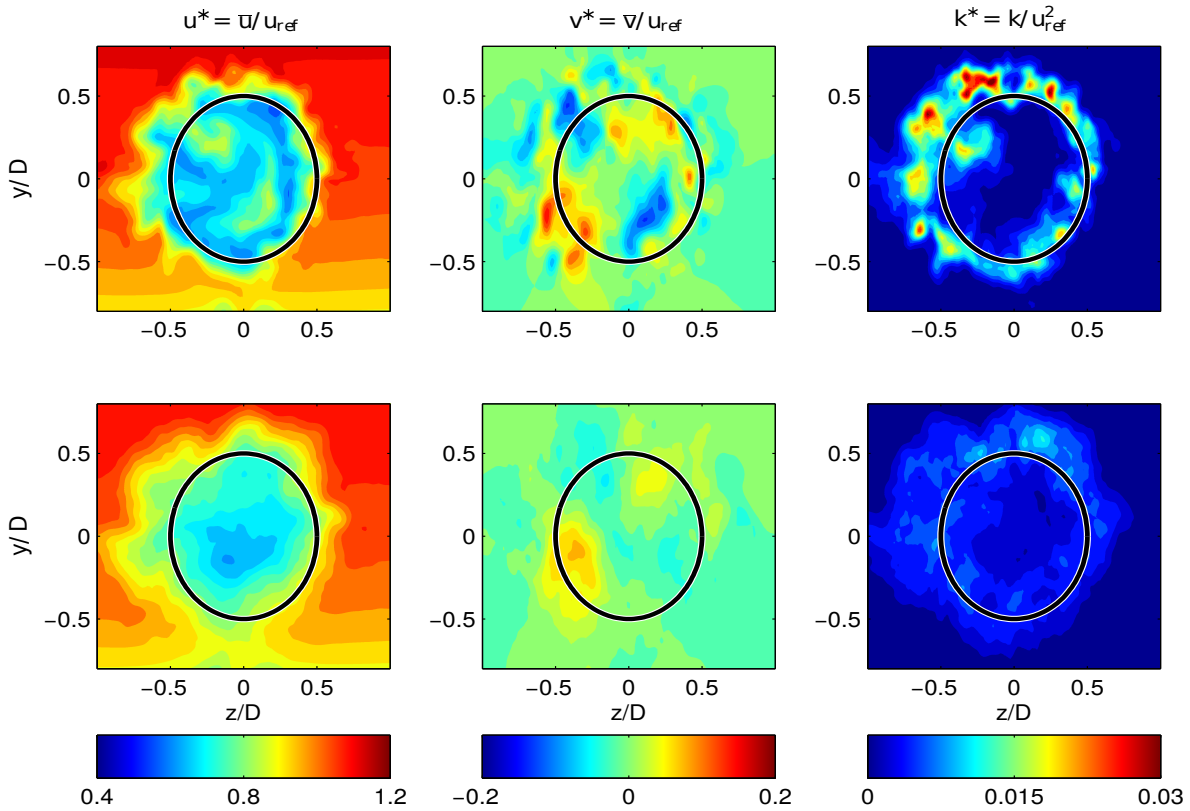

Figure B.3: Different characteristics of the wake in the y - z - plane at the locations x/D = 3 and x/D = 6 of the second case. The black circle pictures the rotor diameter. Top: Location x/D = 3; Bottom: Location x/D = 6; Left: normalized mean streamwise velocity u^*; Middle: normalized mean spanwise velocity v^*; Right: normalized TKE k^*

C. Basics of the physics and geometry

This part of the appendix explains some physical effects, which are needed for the simulations. They are based on Gasch and Twele [2005] and Hansen [2008]. Furthermore, the geometry of the turbine is visualized.

C.1. Momentum - theory

The wind turbine extract kinetic energy E_{ext} from the wind. In this process the area of the stream tube behind the turbine increases and a velocity deficit emerges. This process is pictured in figure C.1.

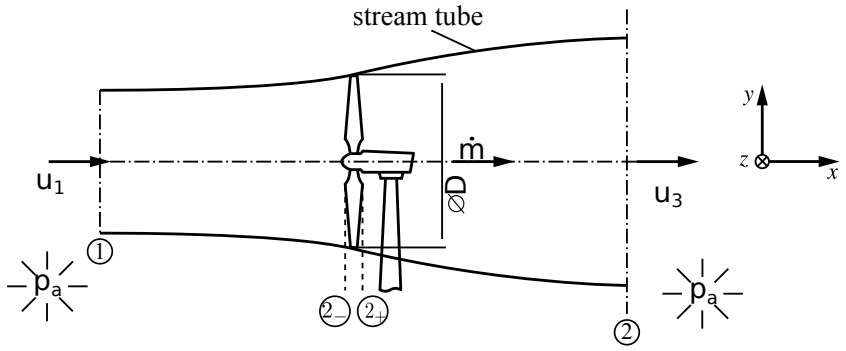

Figure C.1: Momentum theory of a wind turbine

The extract kinetic energy E_{ext} can be calculated as the difference of the kinetic energy in front with the velocity u_1 and the kinetic energy behind with the u_3 the wind turbine (cf. equation C.1).

$$E_{ext} = \frac{1}{2} \cdot m \cdot (u_1^2 - u_3^2) \tag{C.1}$$

The time derivative of E_{ext} is the extract power P_{ext} of the wind with the mass flux $\dot{m}$:

$$P_{ext} = \frac{1}{2} \cdot \dot{m} \cdot (u_1^2 - u_3^2) \tag{C.2}$$

Furthermore, the momentum theory defines the thrust as a product between the mass flux and velocity and on the rotor can be defined as

$$T = \dot{m} \cdot (u_1 - u_3) \tag{C.3}$$

The mass flux $\dot{m}$ is defined in equation C.4 with the area of the rotor A, the density of the air ρ and the velocity in the rotor area u_2.

$$\dot{m} = \rho \cdot A \cdot u_2 \tag{C.4}$$

The pressure and the velocity curve of a wind turbine is displayed in figure C.2. Together with the Bernoulli equation the dynamic and static pressure can be described as:

$$p_1 + \frac{\rho}{2} \cdot u_1^2 = p_{-2} + \frac{\rho}{2} \cdot v_{-2}^2 \tag{C.5}$$

$$p_{2+} + \frac{\rho}{2} \cdot u_{2+}^2 = p_3 + \frac{\rho}{2} \cdot u_3^2 \tag{C.6}$$

The pressure p_1 and p_3 are the same pressure as in the ambience p_a. Based on the infinitesimal thin actuator disk the velocity u_{-2} is equal u_{+2}. The difference between equation C.5 and C.6 is equation C.7

$$\frac{\rho}{2} \cdot (u_1^2 - u_3^2) = p_{-2} - p_{+2} \tag{C.7}$$

Furthermore, the pressure difference on the actuator disk is also defined as the thrust on the rotor

$$T = A \cdot (p_{-2} - p_{+2}) = \frac{\rho}{2} \cdot (u_1^2 - u_3^2) \cdot A \tag{C.8}$$

To figure out the velocity u_2 the equation C.3 can be equated to C.8. The equation C.9 is also named as the "Froude - Rakine - Theorem".

$$u_2 = \frac{u_1 + u_3}{2} \tag{C.9}$$

Together with the "Froude - Rakine - Theorem" the extract power and the thrust can be written as

$$P_{ext} = \frac{1}{2} \cdot \rho \cdot A \cdot u_1^3 \cdot \left(0.5 \cdot \left(1 + \frac{u_3}{u_1}\right) \cdot \left(1 - \frac{u_3}{u_1}\right)^2\right) = \frac{1}{2} \cdot \rho \cdot A \cdot u_1^3 \cdot c_p \tag{C.10}$$

$$T = \rho \cdot A \cdot \frac{u_1 + u_3}{2} \cdot (u_1 - u_3) = c_T \cdot \frac{1}{2} \cdot \rho \cdot u_1^2 \cdot A \tag{C.11}$$

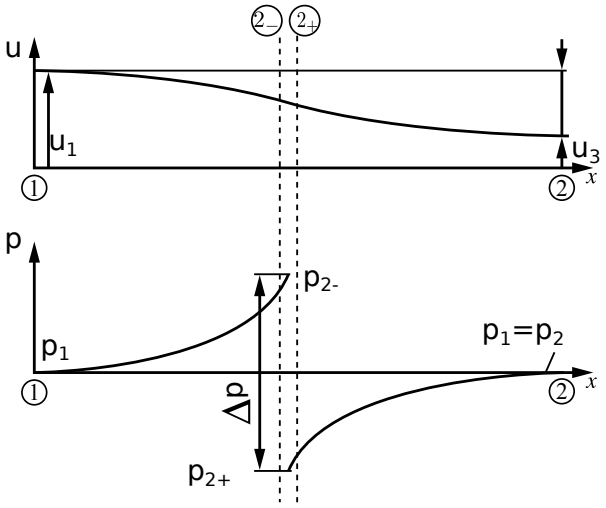

Figure C.2: Top: Velocity in front and behind a turbine, Bottom: Pressure in front and behind a turbine

C.2. Yawed operation

In contrast to the non - yawed turbine, the rotating process of the turbine in yawed operation is divided in down and upstream blades. Based on this difference, an unsteady load affect on the rotor and the pressure drop in figure C.2 is not valid. However, the thrust is generated by the discontinuity pressure drop (cf. equation C.8), which induces a velocity orthogonal to the rotor disk. This velocity deflects the trajectory of the velocity deficit (cf. figure C.3).

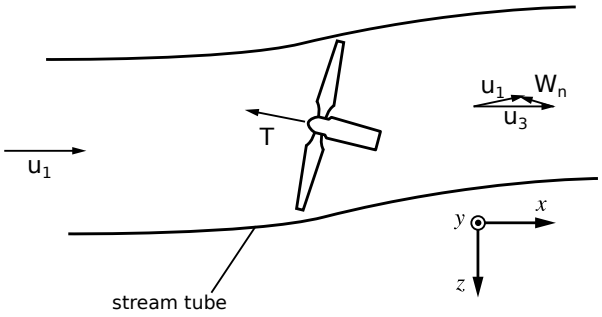

Figure C.3: Top view of a turbine in yawed operation

C.3. Geometry of the wind turbine

In figure C.4 the geometry of the turbine is demonstrated, which is used for the simulations.

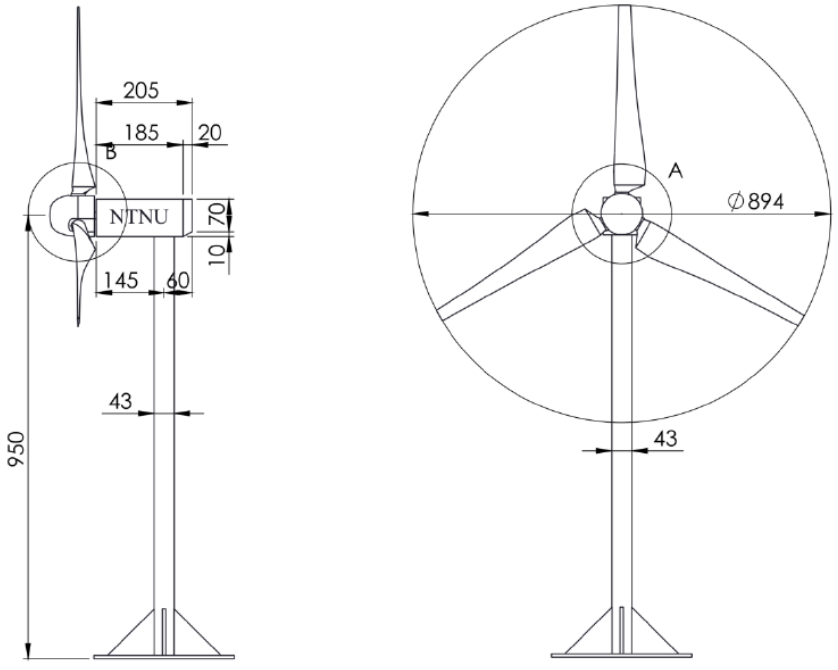

Figure C.4: Geometry of the turbine LARS1 by Sætran et al. [2017]

D. Numerical conditions

In this part of the appendix, the core equations and methods, which are used for the simulations, are listed and explained.

D.1. Navier - Stokes - equations

To calculate the turbulence flow, the incompressible Navier - Stokes - equations are needed. They include the mass flux (equation D.1) and the momentum equations (equation D.2).

$$\frac{\partial}{\partial x_i}(\rho u_i) = 0 \tag{D.1}$$

$$\frac{\partial}{\partial t}(u_i) + \frac{\partial}{\partial x_j}(u_i u_j) = -\frac{1}{\rho} \cdot \frac{\partial p}{\partial x_i} + \nu \frac{\partial^2 u_i}{\partial x_j \partial x_i} \tag{D.2}$$

D.2. Large - Eddy - Simulation

In figure D.1 below the energy is plotted over the frequency in a turbulence flow. This spectrum included three important areas, at the beginning is the production area, in the middle the isotropic area and at the end the dissipation area. The LES simulates the eddies, which transport the energy [Schwarzer, 2014]. Smaller eddies get modulated with a sub - grid and filter technique.

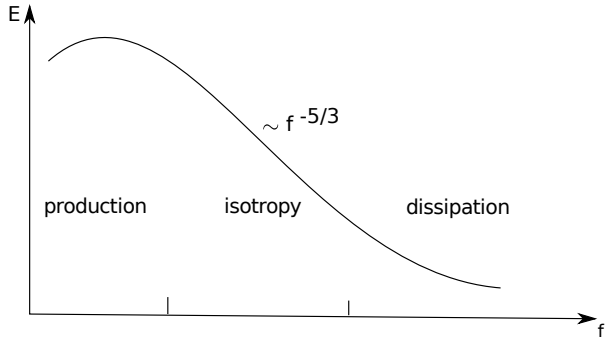

Figure D.1: Energy spectrum of a turbulent flow

The intensive quantities Φ are divided in a low - pass filtered signal $\tilde{\Phi}$ and a high frequency signal Φ' for the LES.

$$\Phi = \widetilde{\Phi} + \Phi'. \tag{D.3}$$

This splitting of the quantities are included in the NST - equation (cf. equation D.1 and D.2). After filtering, the following equations are developed:

$$\frac{\partial}{\partial x_i}\left(\rho\tilde{u}_i\right) = 0 \tag{D.4}$$

$$\frac{\partial}{\partial t}(\tilde{u}_i) + \frac{\partial}{\partial x_j}(\widetilde{u_i u_j}) = -\frac{1}{\rho}\cdot\frac{\partial\tilde{p}}{\partial x_i} + \nu\frac{\partial^2\tilde{u}_i}{\partial x_j\partial x_i} \tag{D.5}$$

The filtered momentum equation can be written as

$$\frac{\partial}{\partial t}(\tilde{u}_i) + \frac{\partial}{\partial x_j}(\tilde{u}_i\tilde{u}_j) = -\frac{1}{\rho}\cdot\frac{\partial\tilde{p}}{\partial x_i} + \nu\frac{\partial^2\tilde{u}_i}{\partial x_j\partial x_i} + \frac{1}{\rho}\frac{\partial\tau_{ij}}{\partial x_j} \tag{D.6}$$

with the sub - grid scal stress tensor $\tau_{ij} = \widetilde{u_i u_j} - \tilde{u}_i\tilde{u}_j$. The quantity $\tilde{\Phi}$ will be divided with an analytical filter function

$$\widetilde{\Phi}_i(x_i) = \int G(x_i - \tau_i)\Phi(\tau_i)d\tau_i. \tag{D.7}$$

D.3. Reynolds - Averaged - Navier - Stokes

Reynolds [1883] divided the intensive quantities in a mean and fluctuation part:

$$\Phi = \overline{\Phi} + \Phi'. \tag{D.8}$$

Similar to the LES, the two parts are included in the NST - equations. After a time average following equations are developed:

$$\frac{\partial}{\partial x_i}\left(\rho\overline{u}_i\right) = 0 \tag{D.9}$$

$$\frac{\partial}{\partial t}(\overline{u}_i) + \frac{\partial}{\partial x_j}(\overline{u_i u_j}) = -\frac{1}{\rho}\cdot\frac{\partial\overline{p}}{\partial x_i} + \nu\frac{\partial^2\overline{u_i}}{\partial x_j\partial x_i} \tag{D.10}$$

The momentum equation can be written as

$$\frac{\partial}{\partial t}(\overline{u}_i) + \frac{\partial}{\partial x_j}(\overline{u}_i\overline{u}_j) = -\frac{1}{\rho}\cdot\frac{\partial\overline{p}}{\partial x_i} + \nu\frac{\partial^2\overline{u_i}}{\partial x_j\partial x_i} + \frac{1}{\rho}\frac{\partial\tau_{ij}^{RS}}{\partial x_j} \tag{D.11}$$

In this case τ_{ij}^{RS} is the Reynolds stress tensor and the reason for the closure problem. Boussinesq [1872] developed a technique to estimate the τ_{ij}^{RS} with the turbulent viscosity ν_T (see equation D.12). The one equation method by Spalart and Allmaras [1994] is based on the turbulent viscosity ν_T.

$$\tau_{ij}^{RS} = \rho\nu_T\cdot\left(\frac{\partial\overline{u_i}}{x_j} + \frac{\partial\overline{u_j}}{x_i}\right) \tag{D.12}$$

D.4. Wall function for the momentum

To reduce the needed computer performance and to accelerate the simulation time, the standard wall function by Launder and Spalding [1974] is applied. This function is a logarithm wall function, which is valid for $30 < y_+ < 300$ (cf. figure D.2).

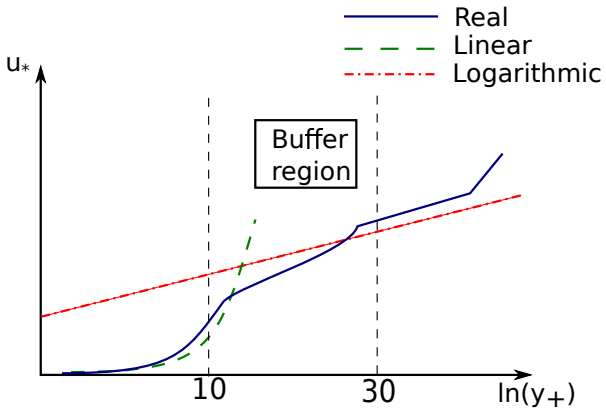

Figure D.2: Wall function

The friction velocity u_* can be calculated with

$$u_* = \frac{1}{\kappa} \cdot ln(E \cdot y_+). \tag{D.13}$$

This velocity depends on the friction in the boundary layer:

$$u_* \equiv \frac{U \cdot C_\mu^{1/4} \cdot k^{1/2}}{\tau_w / \rho} \tag{D.14}$$

and the normalized distance y_+:

$$y_+ \equiv \frac{\rho \cdot C_\mu^{1/4} \cdot k^{1/2} \cdot y}{\mu} \tag{D.15}$$

E. Source - code

In this part of the appendix, the used source for the UDF and POD are listed.

E.1. User-defined functions

```
#include "udf.h"

DEFINE_PROFILE(inlet_x_velocity,thread,position)
{
        real x[ND_ND];
        real y;
        real z;
        face_t f;
        begin_f_loop(f,thread)
                {
                F_CENTROID(x,f,thread);
                F_PROFILE(f,thread,position)= 10*pow(x[1],0.11);
                }
        end_f_loop(f,thread)
}
```

E.2. Matlab - POD

```
%% Matlab POD - code for coherent velocity
%% Import data of the location x/D = 1, 3 and 6.
start1= ;
anzahl1= ;
k=0;
for n=start1:anzahl1
k=k+1
filename=['x_D-1-' num2str(n,'%0.4d')];
x_D_1=importdata(filename);
M1c2(:,k)=[x_D_1.data(:,9)]; % streamwise velocity
end
x_1=x_D_1.data(:,2);
y_1=(x_D_1.data(:,3)-0.9)./0.9;
z_1=x_D_1.data(:,4)./(-0.9);
[z1,y1]=meshgrid(linspace(-1,1,270*10),linspace
    (-0.8,0.8,180*10)); % interpolation to generate a uniform
    grid
mittel1c=mean(M1c2,2);

```

```
18 start3= ;
19 anzahl3= ;
20 k=0;
21 for n=start3:anzahl3
22 k=k+1
23 filename=['x_D-3-' num2str(n,'%0.4d')];
24 x_D_3=importdata(filename);
25 M3c(:,k)=x_D_3.data(:,9);
26 end
27 x_3=x_D_3.data(:,2);
28 y_3=(x_D_3.data(:,3)-0.9)./0.9;
29 z_3=x_D_3.data(:,4)./(-0.9);
30 [z3,y3]=meshgrid(linspace(-1,1,270*10),linspace
      (-0.8,0.8,180*10));
31 mittel3c=mean(M3c,2);
32 Mittel3=griddata(z_3,y_3,mittel3,z3,y3,'linear');
33
34 start6= ;
35 anzahl6= ;
36 k=0;
37 for n=start6:anzahl6
38 k=k+1
39 filename=['x_D-6-' num2str(n,'%0.4d')];
40 x_D_6=importdata(filename);
41 M6c(:,k)=x_D_6.data(:,9);
42 end
43 x_6=x_D_6.data(:,2);
44 y_6=(x_D_6.data(:,3)-0.9)./0.9;
45 z_6=x_D_6.data(:,4)./(-0.9);
46 [z6,y6]=meshgrid(linspace(-1,1,270*10),linspace
      (-0.8,0.8,180*10));
47 mittel6c=mean(M6c,2);
48
49 %% SVD of the snapshot matrix M
50
51 M1c=M1c2-kron(ones(1,anzahl1-start1+1),mittel1c);
52 [U1,S1,V1]=svd(M1c,'econ');
53 sigma1=diag(S1);
54
55 M3c=M3c-kron(ones(1,anzahl3-start3+1),mittel3c);
56 [U3,S3,V3]=svd(M3c,'econ');
57 sigma3=diag(S3);
58
59 M6c=M6c-kron(ones(1,1810),mittel6c);
```

```
60  [U6,S6,V6]=svd(M6c,'econ');
61  sigma6=diag(S6);
62
63  %% Generation of the time modes and phase angle
64
65   V12Norm=sqrt(V1(:,1).^2+V1(:,2).^2);
66   V1Norm=V1(:,1)./V12Norm;
67   V2Norm=V1(:,2)./V12Norm;
68
69   V312Norm=sqrt(V3(:,1).^2+V3(:,2).^2);
70   V31Norm=V3(:,1)./V312Norm;
71   V32Norm=V3(:,2)./V312Norm;
72
73   V612Norm=sqrt(V6(:,1).^2+V6(:,2).^2);
74   V61Norm=V6(:,1)./V612Norm;
75   V62Norm=V6(:,2)./V612Norm;
76
77   Phase12=atan2(V1Norm,V2Norm);
78   Phase312=atan2(V31Norm,V32Norm);
79   Phase612=atan2(V61Norm,V62Norm);
80
81   %% Calculation of the phase average and the coherent structure
82   NPhase=25;
83   for i=-NPhase:NPhase
84       Maske=(Phase12>pi*i/NPhase) & (Phase12<=pi*(i+1)/NPhase);
85       P(:,i+NPhase+1)=sum(M1c(:,Maske),2)/sum(Maske);
86   end
87   clear Maske
88    for i=-NPhase:NPhase
89       Maske=(Phase312>pi*i/NPhase) & (Phase312<=pi*(i+1)/NPhase)
             ;
90       P3(:,i+NPhase+1)=sum(M3c(:,Maske),2)/sum(Maske);
91    end
92    clear Maske
93    for i=-NPhase:NPhase
94       Maske=(Phase612>pi*i/NPhase) & (Phase612<=pi*(i+1)/NPhase)
             ;
95       P6(:,i+NPhase+1)=sum(M6c(:,Maske),2)/sum(Maske);
96   end
97  KO=griddata(z_1,y_1,P(:,1),z1,y1,'linear');
98  KO3=griddata(z_3,y_3,P3(:,1),z3,y3,'linear');
99  KO6=griddata(z_6,y_6,P6(:,1),z6,y6,'linear');
```